Plato's cube and the natural geometry of fragmentation

Gábor Domokos[a,b], Douglas J. Jerolmack[c,d,1], Ferenc Kun[e], and János Török[a,f]

[a]MTA-BME Morphodynamics Research Group, Budapest University of Technology and Economics, 1111 Budapest, Hungary; [b]Department of Mechanics, Materials and Structure, Budapest University of Technology and Economics, 1111 Budapest, Hungary; [c]Department of Earth and Environmental Science, University of Pennsylvania, Philadelphia, PA 19104; [d]Mechanical Engineering and Applied Mechanics, University of Pennsylvania, Philadelphia, PA 19104; [e]Department of Theoretical Physics, University of Debrecen, 4032 Debrecen, Hungary; and [f]Department of Theoretical Physics, Budapest University of Technology and Economics, 1111 Budapest, Hungary

Edited by David A. Weitz, Harvard University, Cambridge, MA, and approved May 27, 2020 (received for review January 17, 2020)

Plato envisioned Earth's building blocks as cubes, a shape rarely found in nature. The solar system is littered, however, with distorted polyhedra—shards of rock and ice produced by ubiquitous fragmentation. We apply the theory of convex mosaics to show that the average geometry of natural two-dimensional (2D) fragments, from mud cracks to Earth's tectonic plates, has two attractors: "Platonic" quadrangles and "Voronoi" hexagons. In three dimensions (3D), the Platonic attractor is dominant: Remarkably, the average shape of natural rock fragments is cuboid. When viewed through the lens of convex mosaics, natural fragments are indeed geometric shadows of Plato's forms. Simulations show that generic binary breakup drives all mosaics toward the Platonic attractor, explaining the ubiquity of cuboid averages. Deviations from binary fracture produce more exotic patterns that are genetically linked to the formative stress field. We compute the universal pattern generator establishing this link, for 2D and 3D fragmentation.

Gömböc | statistical physics | fracture mechanics | pattern formation

Solids are stressed to their breaking point when growing crack networks percolate through the material (1, 2). Failure by fragmentation may be catastrophic (1, 3) (Fig. 1), but this process is also exploited in industrial applications (4). Moreover, fragmentation of rock and ice is pervasive within planetary shells (1, 5, 6) and creates granular materials that are literally building blocks for planetary surfaces and rings throughout the solar system (6–10) (Fig. 1). Plato postulated that the idealized form of Earth's building blocks is a cube, the only space-filling Platonic solid (11, 12). We now know that there is a zoo of geometrically permissible polyhedra associated with fragmentation (13) (Fig. 2). Nevertheless, observed distributions of fragment mass (14–17) and shape (18–21) are self-similar, and models indicate that geometry (size and dimensionality) matters more than energy input or material composition (16, 22, 23) in producing these distributions.

Fragmentation tiles the Earth's surface with telltale mosaics. Jointing in rock masses forms three-dimensional (3D) mosaics of polyhedra, often revealed to the observer by two-dimensional (2D) planes at outcrops (Fig. 2). The shape and size of these polyhedra may be highly regular, even approaching Plato's cube, or resemble a set of random intersecting planes (24). Alternatively, quasi-2D patterns, such as columnar joints, sometimes form in solidification of volcanic rocks (25). These patterns have been reproduced in experiments of mud and corn-starch cracks, model 2D fragmentation systems, where the following have been observed: Fast drying produces strong tension that drives the formation of primary (global) cracks that criss-cross the sample and make "X" junctions (25–27) (Fig. 3); slow drying allows the formation of secondary cracks that terminate at "T" junctions (26); and "T" junctions rearrange into "Y" junctions (25, 28) to either maximize energy release as cracks penetrate the bulk (29–31) or during reopening–healing cycles from wetting/drying (32) (Fig. 3). Whether in rock, ice, or soil, the fracture mosaics cut into stressed landscapes (Fig. 3) form pathways for focused fluid flow, dissolution, and erosion that further disintegrate these materials (33, 34) and reorganize landscape patterns (35, 36). Moreover, fracture patterns in rock determine the initial grain size of sediment supplied to rivers (36, 37).

Experiments and simulations provide anecdotal evidence that the geometry of fracture mosaics is genetically related to the formative stress field (38). It is difficult to determine, however, if similarities in fracture patterns among different systems are more than skin-deep. First, different communities use different metrics to describe fracture mosaics and fragments, inhibiting comparison among systems and scales. Second, we do not know whether different fracture patterns represent distinct universality classes or are merely descriptive categories applied to a pattern continuum. Third, it is unclear if and how 2D systems map to 3D.

Here, we introduce the mathematical framework of convex mosaics (39) to the fragmentation problem. This approach relies on two key principles: that fragment shape can be well approximated by convex polytopes (24) (2D polygons and 3D polyhedra; Fig. 2*A*) and that these shapes must fill space without gaps, since

Significance

We live on and among the by-products of fragmentation, from nanoparticles to rock falls to glaciers to continents. Understanding and taming fragmentation is central to assessing natural hazards and extracting resources, and even for landing probes safely on other planetary bodies. In this study, we draw inspiration from an unlikely and ancient source: Plato, who proposed that the element Earth is made of cubes because they may be tightly packed together. We demonstrate that this idea is essentially correct: Appropriately averaged properties of most natural 3D fragments reproduce the topological cube. We use mechanical and geometric models to explain the ubiquity of Plato's cube in fragmentation and to uniquely map distinct fragment patterns to their formative stress conditions.

Author contributions: G.D. designed research; G.D., F.K., and J.T. performed research; G.D., D.J.J., F.K., and J.T. contributed new reagents/analytic tools; G.D., D.J.J., F.K., and J.T. analyzed data; and G.D., D.J.J., F.K., and J.T. wrote the paper.

The authors declare no competing interests.

This article is a PNAS Direct Submission.

Data deposition: Shape and mass data for all measured 3D rock fragments, including both the small and large experimental datasets, are freely available at the Center for Open Science (https://osf.io/h2ezc/). All code for the geometric simulations—i.e., the cut and break models—is free to download from GitHub (https://github.com/torokj/Geometric_fragmentation).

[1]To whom correspondence may be addressed. Email: sediment@sas.upenn.edu.

This article contains supporting information online at https://www.pnas.org/lookup/suppl/doi:10.1073/pnas.2001037117/-/DCSupplemental.

First published July 17, 2020.

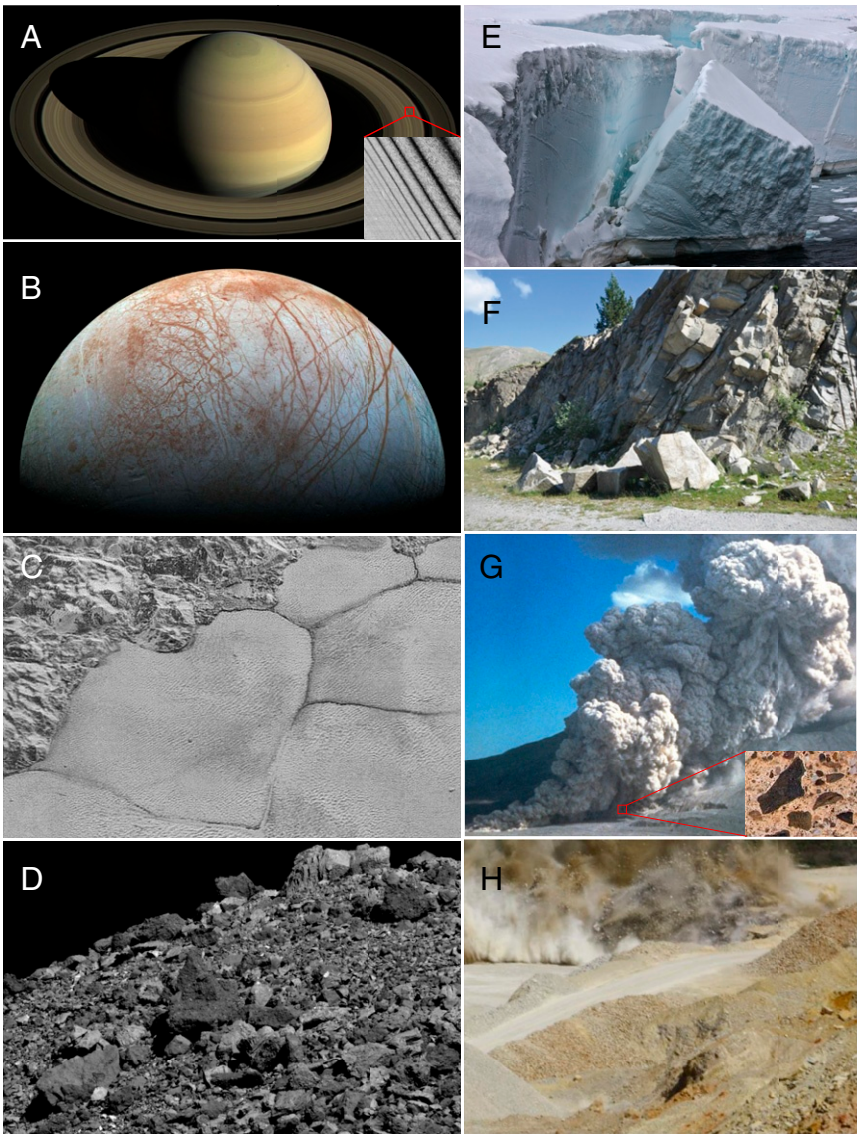

Fig. 1. Fragmentation across planets and scales. *A–D* show planetary surfaces and rings. (*A*) Saturn's rings composed of ice (*Inset*). Image credit: NASA/JPL-Caltech/Space Science Institute. (*B*) Jupiter's moon Europa showing cracked planetary shell. Image credit: NASA/JPL-Caltech/SETI Institute. (*C*) Polygonal cracks on Pluto. Image credit: NASA/JHUAPL/SwRI. (*D*) Surface of the asteroid Bennu. Image credit: NASA/Goddard/University of Arizona. *E–H* show example processes forming fragments on Earth. (*E*) Iceberg calving. Image credit: Australian Antarctic Division/Ian Phillips. (*F*) Rock falls. Reproduced from ref. 58, which is licensed under CC BY 4.0. (*G*) Volcanic eruptions that produce pyroclastic flows, forming breccia deposits (*Inset*). Image credit: US Geological Survey/Peter Lipman. *Inset* image credit: Siim Sepp (http://www.sandatlas.org/). (*H*) Mine blasting. Image credit: Sarolta Bodor (photographer).

fragments form by the disintegration of solids. Without loss of generality (*SI Appendix*, section 1.1), we choose a model that ignores the local texture of fracture interfaces (40, 41). Fragments can then be regarded as the cells of a convex mosaic (39), which may be statistically characterized by three parameters. *Cell degree* ($\bar{v}$) is the average number of vertices of the polytopes, and *nodal degree* ($\bar{n}$) is the average number of vertices that meet at a node (42): We call $[\bar{n}, \bar{v}]$ the *symbolic plane*. We define the third parameter $0 \leq p \equiv N_R/(N_R + N_I) \leq 1$ as the *regularity* of the mosaic. N_R is the number of *regular* nodes in which cell vertices only coincide with other vertices, corresponding in 2D to "X" and "Y" junctions with $n = 4$ and 3, respectively. N_I is the number of irregular nodes where vertices lie along edges (2D) or faces (3D) of other cells, corresponding in 2D to "T" junctions of $n = 2$ (Fig. 2*B*). We define regular and irregular mosaics as having $p = 1$ and $p = 0$, respectively. For 3D mosaics, we also introduce $\bar{f}$ as the average number of faces. In contrast to other descriptions of fracture networks (24), our framework does not delineate stochastic from deterministic mosaics; networks made from random or periodic fractures may have identical parameter values (Fig. 3). This theory provides a global chart of geometrically admissible 2D and 3D mosaics in the symbolic plane. Although we focus here on mosaics formed by fracture, these global charts include all geometrically possible mosaics, including human-made ones.

In this paper, we measure the geometry of a wide variety of natural 2D fracture mosaics and 3D rock fragments and find that they form clusters within the global chart. Remarkably, the most significant cluster corresponds to the "Platonic attractor": fragments with cuboid averages. Discrete element method (DEM) simulations of fracture mechanics show that cuboid averages emerge from primary fracture under the most generic stress field. Geometric simulations show how secondary fragmentation by binary breakup drives any initial mosaic toward cuboid averages.

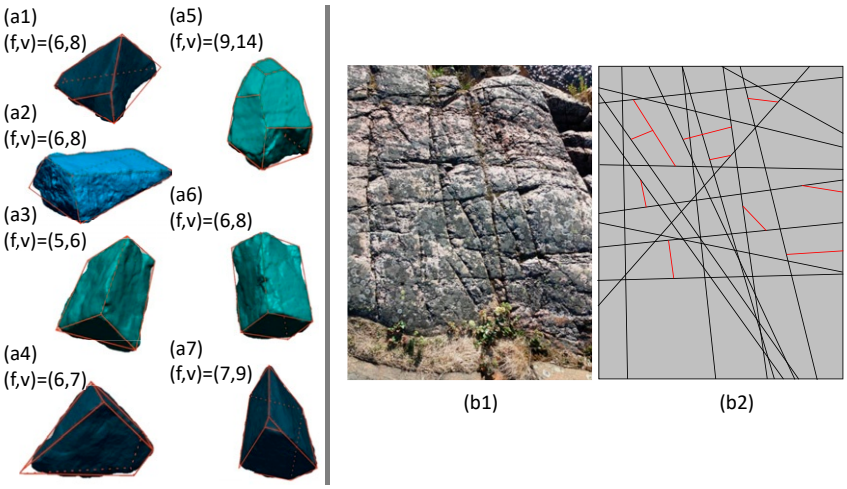

Fig. 2. Examples of fragments and fracture lines. (*A*) Natural fragments approximated by convex polyhedra. (*B*, *1*) Granite wall showing global cracks. (*B*, *2*) Approximation of fragmentation pattern by regular primitive mosaic (black lines) and its irregular version with secondary cracks (red lines).

The 2D Mosaics in Theory and in Nature. The geometric theory of 2D convex mosaics is essentially complete (39) and is given by the formula (42)

$$\bar{v} = \frac{2\bar{n}}{\bar{n} - p - 1}, \qquad [1]$$

which delineates the admissible domain for convex mosaics within the $[\bar{n}, \bar{v}]$ symbolic plane (Fig. 3)—i.e., the global chart. Boundaries on the global chart are given by: 1) the $p = 1$ and $p = 0$ lines; and 2) the overall constraints that the minimal degree of regular nodes and cells is three, while the minimal degree of irregular nodes is two. We constructed geometric simulations of a range of stochastic and deterministic mosaics (*SI Appendix*, section 2) to illustrate the continuum of patterns contained within the global chart (Fig. 3)

We describe two important types of mosaics, which help to organize natural 2D patterns. First are *primitive mosaics*, patterns formed by binary dissection of domains. If the dissection is global, we have *regular primitive mosaics* ($p = 1$) composed entirely of straight lines, which, by definition, bisect the entire sample. These mosaics occupy the point $[\bar{n}, \bar{v}] = [4, 4]$ in the symbolic plane (39). In nature, the straight lines appear as primary, global fractures. Next, we consider the situation where the cells of a regular primary mosaic are sequentially bisected locally. Irregular (T-type) nodes are created resulting in a progressive decrease $p \to 0$ and concomitant decrease $\bar{n} \to 2$ toward an *irregular primitive mosaic*. The value $\bar{v} = 4$, however, is unchanged by this process (Fig. 3), so in the limit, we arrive at $[\bar{n}, \bar{v}] = [2, 4]$. In nature, these local bisections correspond to secondary fracturing (3, 38). Fragments produced from primary vs. secondary fracture are indistinguishable. Further, any initial mosaic subject

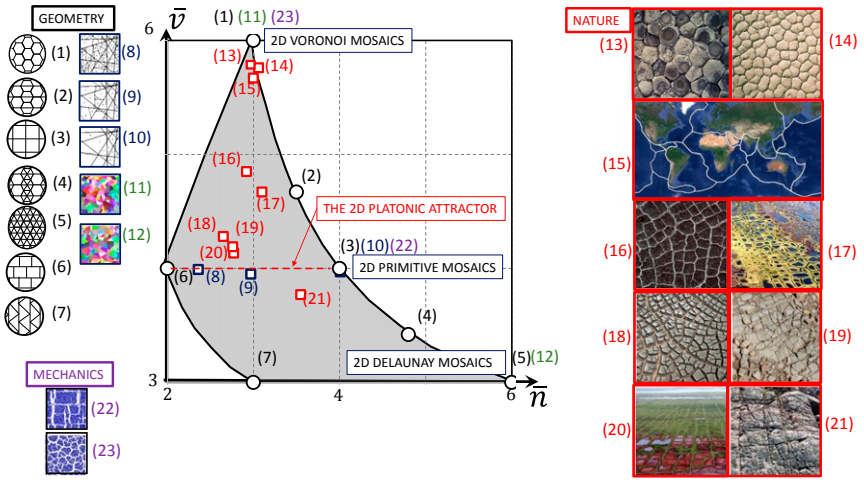

Fig. 3. Mosaics in 2D. (*Left*) Symbolic plane $[\bar{n}, \bar{v}]$ with geometrically admissible domain (defined in Eq. **1**) shaded gray. Patterns 1 to 7 marked with black circles are deterministic periodic patterns. Patterns 8 to 12 are geometric simulations of random mosaics: 8, regular primitive; 9 and 10, advanced (irregular) primitive; 11, Poisson–Voronoi; and 12, Poisson–Delaunay. (*Right*) Red squares (13 to 21) correspond to analyzed images of natural 2D mosaics shown: 13, columnar joints, Giant's Causeway (Image credit: Japan Society for the Promotion of Science–UK Research and Innovation Joint Research Project/Akio Nakahara); 14, mud cracks (Image credit: Charles E. Jones [University of Pittsburgh, Pittsburgh, PA]); 15, tectonic plates; 16, Martian surface (Image credit: NASA/JPL-Caltech/University of Arizona); 17, permafrost in Alaska (Image credit: Matthew L. Druckenmiller [University of Colorado Boulder, Boulder, CO]); 18, mud cracks (Image credit: Hannes Grobe [Alfred Wegener Institute, Bremerhaven, Germany]); 19, dolomite outcrop; 20, permafrost in Alaska (Image credit: Bretwood Higman [photographer]); and 21, granite rock surface. Patterns 22 and 23 are generated by generic DEM simulation (*Materials and Methods*): 22, general stress state with eigenvalues $\sigma_1 > \sigma_2$; and 23, isotropic stress state with $\sigma_1 = \sigma_2$.

to secondary splitting of cells will, in the limit, produce fragments with $\bar{v}=4$ (*SI Appendix*, section 1). Thus, we expect primitive mosaics associated with the line $\bar{v}=4$ in the global chart to be an attractor in 2D fragmentation, as noted by ref. 43, and we expect the average angle to be a rectangle (26) (Fig. 2). We call this the Platonic attractor. As a useful aside, a planar section of a 3D primitive mosaic (e.g., a rock outcrop) is itself a 2D primitive mosaic (Fig. 2). The second important pattern is *Voronoi mosaics*, which are, in the averaged sense, hexagonal tilings $[\bar{n},\bar{v}]=[3,6]$. They occupy the peak of the 2D global chart (Fig. 3).

We measured a variety of natural 2D mosaics (*SI Appendix*, section 2) and found, encouragingly, that they all lie within the global chart permitted by Eq. **1**. Mosaics close to the Platonic ($\bar{v}=4$) line include patterns known or suspected to arise under primary and/or secondary fracture: jointed rock outcrops, mud cracks, and polygonal frozen ground. Mosaics close to Voronoi include mud cracks and, most intriguingly, Earth's tectonic plates. Hexagonal mosaics are known to arise in the limit for systems subject to repeated cycles of fracturing and healing (25) (Fig. 3). We thus consider Voronoi mosaics to be a second important attractor in 2D. Horizontal sections of columnar joints also belong to this geometric class; however, their evolution is inherently 3D, as we discuss below.

It is known that Earth's tectonic plates meet almost exclusively at "Y" junctions; there is debate, however, about whether this "Tectonic Mosaic" formed entirely from surface fragmentation or contains a signature of the structure of mantle dynamics underneath (5, 44, 45). We examine the tectonic plate configuration (45) as a 2D convex mosaic, treating the Earth's crust as a thin shell. We find $[\bar{n},\bar{v}]=[3.0,5.8]$, numbers that are remarkably close to a Voronoi mosaic. Indeed, the slight deviation from $[\bar{n},\bar{v}]=[3,6]$ is because the Earth's surface is a spherical manifold, rather than planar (*SI Appendix*, section 2.3). While this analysis doesn't solve the surface/mantle question, the geometry of the Tectonic Mosaic is compatible with either 1) an evolution consisting of episodes of brittle fracture and healing or 2) cracking via thermal expansion.

The rest of our observed natural 2D mosaics plot between the Platonic and Voronoi attractors (Fig. 3). We suspect that these landscape patterns, which include mud cracks and permafrost, either initially formed as regular primitive mosaics and are in various stages of evolution toward the Voronoi attractor; or were Voronoi mosaics that are evolving via secondary fracture toward the Platonic attractor. For the case of mosaics in permafrost, however, we acknowledge that mechanisms other than fracture—such as convection—could also be at play.

Extension to 3D Mosaics. There is no formula for 3D convex mosaics analogous to the $p=1$ line of Eq. **1** that defines the global chart. There exists a conjecture, however, with a strong mathematical basis (42); at present, this conjecture extends only to regular mosaics. We define the *harmonic degree* as $\bar{h}=\bar{n}\bar{v}/(\bar{n}+\bar{v})$. The conjecture is that $d<\bar{h}\le 2^{d-1}$, where d is system dimension. For 2D mosaics, we obtain the known result (39, 42) $\bar{h}=2$, consistent with the $p=1$ substitution in Eq. **1**. In 3D, the conjecture is equivalent to $3<\bar{h}\le 4$, predicting that all regular 3D convex mosaics live within a narrow band in the symbolic $[\bar{n},\bar{v}]$ plane (42) (Fig. 4). Plotting a variety of well-studied periodic and random 3D mosaics (*SI Appendix*, section 3), we confirm that all of them are indeed confined to the predicted 3D global chart (Fig. 4). Unlike the 2D case, we cannot directly measure $\bar{n}$ in most natural 3D systems. We can, however, measure the polyhedral cells (the fragments): the average numbers $\bar{f},\bar{v}$ of faces and vertices, respectively. Values for $[\bar{f},\bar{v}]$ may be plotted in what we call the *Euler plane*, where the lines bounding the permissible domain correspond to simple polyhedra (upper) where vertices are adjacent to three edges

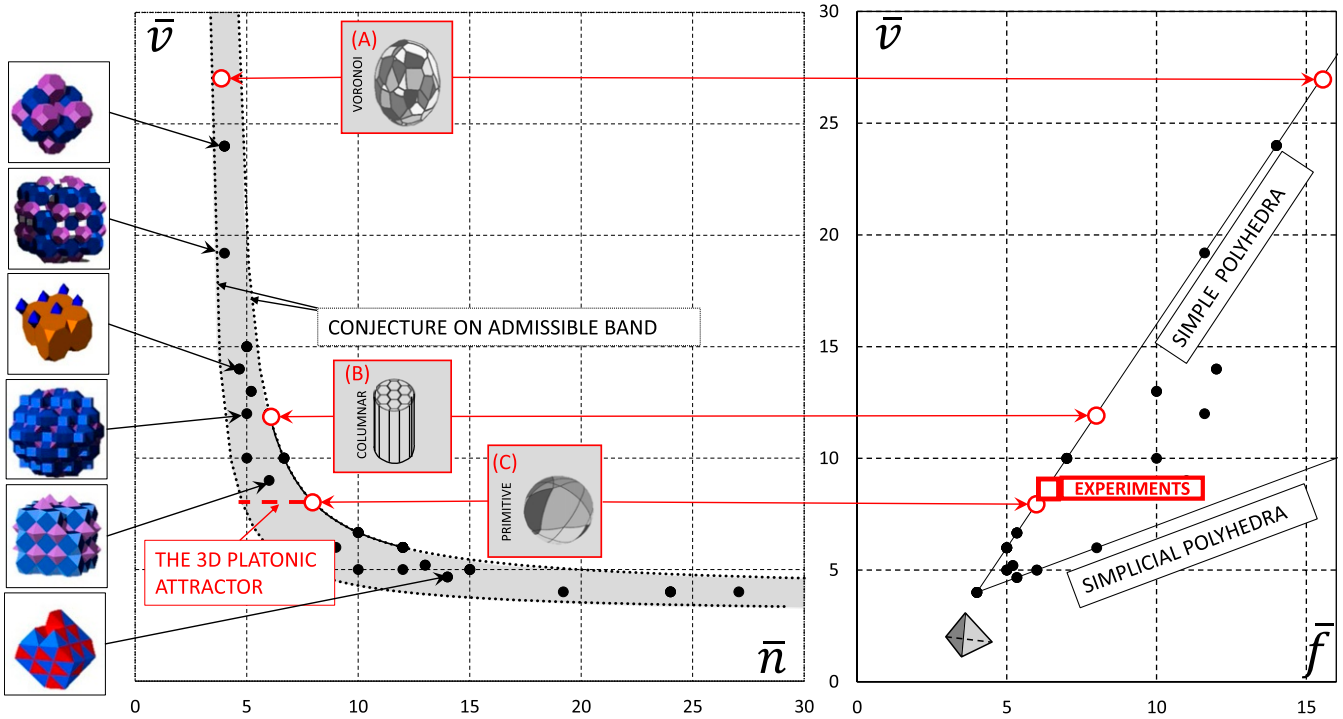

Fig. 4. Mosaics in 3D. A total of 28 uniform honeycombs, their duals, Poisson–Voronoi, Poisson–Delaunay, and primitive random mosaics plotted on the parameter planes. (*Left*) The $[\bar{n},\bar{v}]$ plane, where continuous black line corresponds to prismatic mosaics (42). The shaded gray area marks the predicted domain based on the conjecture $d<\bar{h}\le 2^{d-1}$. (*Right*) The $[\bar{f},\bar{v}]$ plane, where straight black lines correspond to simple polyhedra (top) and their duals (bottom); for the tetrahedron $[\bar{f},\bar{v}]=[4,4]$, these two are identical. Mosaics highlighted in Fig. 5 are marked by red circles on both panels: 3D Voronoi (A); columnar mosaics (B); and 3D primitive mosaic (C).

and three faces, and their dual polyhedra which have triangular faces (lower; Fig. 4). Simple polyhedra arise as cells of mosaics in which the intersections are generic—i.e., at most three planes intersect at one point—and this does not allow for odd values of v.

As in 2D, 3D regular primitive mosaics are created by intersecting global planes. These mosaics occupy the point $[\bar{n}, \bar{v}] = [8, 8]$ on the 3D global chart (Fig. 4). Cells of regular primitive mosaics have cuboid averages $[\bar{f}, \bar{v}] = [6, 8]$ (39, 42). This is the Platonic attractor, marked by the $\bar{v} = 8$ line in the global chart. The 3D Voronoi mosaics, similar to their 2D counterparts, are associated with the Voronoi tessellation defined by some random process. If the latter is a Poisson process, then we obtain (39) $[\bar{n}, \bar{v}] = [4, 27.07], [\bar{f}, \bar{v}] = [15.51, 27.07]$ (Fig. 4).

Prismatic mosaics are created by regarding the 2D pattern as a base that is extended in the normal direction. The prismatic mosaic constructed from a 2D primitive mosaic has cuboid averages and is therefore statistically equivalent to a 3D primitive mosaic. The prismatic mosaic created from a 2D Voronoi base is what we call a *columnar mosaic*, and it has distinct statistical properties: $[\bar{n}, \bar{v}] = [6, 12], [\bar{f}, \bar{v}] = [8, 12]$. Thus, the three main natural extensions of the two dominant 2D patterns are 3D primitive, 3D Voronoi, and columnar mosaics.

Regular primitive mosaics appear to be the dominant 3D pattern resulting from primary fracture of brittle materials (46). Moreover, dynamic brittle fracture produces binary breakup in secondary fragmentation (23, 47), driving the 3D averages $[\bar{f}, \bar{v}]$ toward the Platonic attractor. The most common example in nature is fractured rock (Figs. 2 and 4). The other two 3D mosaics are more exotic and seem to require more specialized conditions to form in nature. Columnar joints like the celebrated Giants Causeway, formed by the cooling of large basaltic rock masses (25, 31, 48) (Fig. 5*B*), appear to correspond to columnar mosaics. In these systems, the hexagonal arrangement and downward (normal) penetration of cracks arise as a consequence of maximizing energy release (29–31). The only potential examples of 3D Voronoi mosaics that we know of are septarian nodules, such as the famous Moeraki Boulders (49) (Fig. 4). These enigmatic concretions have complex growth and compaction histories and contain internal cracks that intersect the surface (50). Similar to primitive mosaics, the intersection of 3D Voronoi mosaics with a surface is a 2D Voronoi mosaic.

Connecting Primary Fracture Patterns to Mechanics with Simulations. We hypothesize that primary fracture patterns are genetically linked to distinct stress fields, in order of most generic to most rare. In a 2D homogeneous stress field, we may describe the stress tensor with eigenvalues $|\sigma_1| \geq |\sigma_2|$ and characterize the stress state by the dimensionless parameters $\mu = \sigma_2/\sigma_1$ and $i = \mathrm{sgn}(\sigma_1)$, whose admissible domain is $\mu \in [-1, 1]$ (and it is double covered due to $i = \pm 1$). In 3D, this corresponds to eigenvalues $|\sigma_1| \geq |\sigma_2| \geq |\sigma_3|$, stress state $\mu_1 = \sigma_2/\sigma_1, \mu_2 = \sigma_3/\sigma_1, i = \mathrm{sgn}(\sigma_1)$, and domain $\mu_1, \mu_2 \in [-1, 1], |\mu_1| \geq |\mu_2|$ (and it is double covered due to $i = \pm 1$) (Fig. 5). There is a unique map from these stress-field parameters to the location of the resultant fracture mosaics in the global chart; we call this map the mechanical *pattern generator*. [Results may be equivalently cast on the Flinn diagram (51) commonly used in structural geology: *SI Appendix*, Fig. S10]. The 2D pattern generator is described by the single scalar function $\bar{v}(\mu, i)$ (and $\bar{n}$ can be computed from Eq. **1**), while the 3D pattern generator is characterized by scalar functions $\bar{n}(\mu_1, \mu_2, i), \bar{v}(\mu_1, \mu_2, i), \bar{f}(\mu_1, \mu_2, i)$. Computing the full pattern generator is beyond the scope of the current paper, even in 2D. Instead, we perform generic DEM simulations (52, 53) of a range of scenarios to interpret the important primary mosaic patterns described above (*Materials and Methods*).

In 2D, we find that pure shear produces regular primitive mosaics (Fig. 3), implying $\bar{v}(-1, \pm 1) \approx 4$. This corresponds to the Platonic attractor. In contrast, hydrostatic tension creates regular Voronoi mosaics (Fig. 3 and *SI Appendix*, section 4), such that $\bar{v}(1, 1) \approx 6$—the Voronoi attractor. Both are in agreement with our expectations.

In 3D, we first conducted DEM simulations of hard materials at $[\mu_1, \mu_2]$ locations corresponding to shear, uniform 2D tension and uniform 3D tension ($[-0.5, -0.25]$, $[1, -0.2]$ and $[1, 1]$, respectively) (*Materials and Methods* and *SI Appendix*, section 4). The resulting mosaics displayed the expected fracture patterns for brittle materials: primitive, columnar, and Voronoi, respectively (Fig. 5). To obtain a global, albeit approximate, picture of the 3D pattern generator, we ran additional DEM simulations

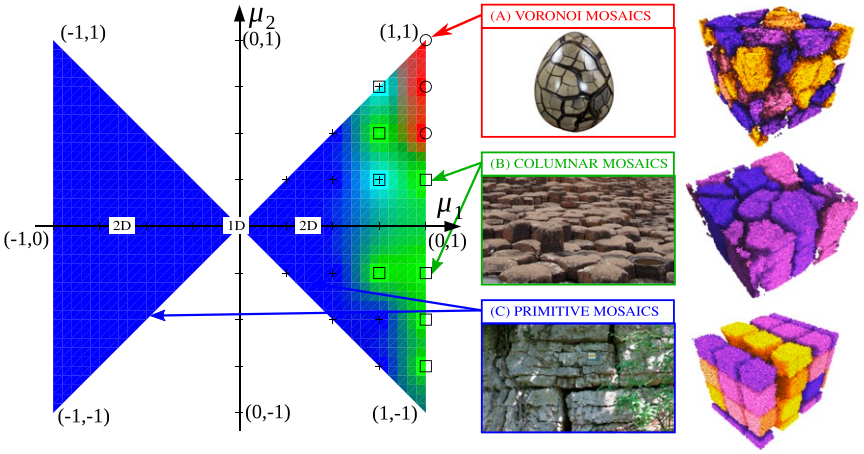

Fig. 5. Illustration of the 3D pattern generator. (*Left*) The $i = 1$ leaf of the $[\mu_1, \mu_2]$ plane. Colors (symbols) indicate patterns observed in 74 DEM simulations; marked lattice points are associated with multiple simulations. Blue plus, primitive; green square, columnar; and red circle, Voronoi. Overlapping colors (symbols) indicate intermediate mosaic patterns. (*Right*) Simulation and field examples. (*A*) A 3D Voronoi-type mosaic at $\mu_1 = \mu_2 = i = 1$; observe surface patterns on all planar sections agreeing with 2D Voronoi-type tessellations, and also with surface patterns of the shown septarian nodule. Image credit: FossilEra/Matt Heaton. (*B*) Columnar mosaic at $\mu_1 = 1, \mu_2 = 0, i = 1$; surface pattern on horizontal section is a 2D Voronoi-type tessellation, while parallel vertical lines extend normal to the surface, both matching observations on the illustrated basalt columnar joints. Image credit: Japan Society for the Promotion of Science–UK Research and Innovation Joint Research Project/Akio Nakahara. (*C*) A 3D primitive mosaic at $\mu_1 = -0.5$, $\mu_2 = -0.25$, and $i = 1$; note surface patterns on all sections agree with 2D primitive mosaics, and also correspond to fracture patterns on the illustrated rock.

that uniformly sampled the stress space on a 9×9 ($\Delta\mu = 0.25$) grid, for both $i = +1$ and $i = -1$ (*SI Appendix*, section 4). The constructed pattern generator demarcated the boundaries in stress-state space that separate the three primary fracture patterns (Fig. 5). The vast proportion of this space is occupied by primitive mosaics, which are also the only pattern generated under negative volumetric stress. Such compressive stress conditions are pervasive in natural rocks. Columnar mosaics are a distant second in terms of frequency of occurrence; they occupy a narrow stripe in the stress space. Most rare are Voronoi mosaics, which only occur in a single corner of the stress space (Fig. 5). Boundaries separating the three patterns shifted somewhat for simulations that used softer materials (*SI Appendix*, Fig. S9), but the ranking did not. These primary fracture mosaics serve as initial conditions for secondary fracture. While our DEM simulations do not model secondary fracture, we remind the reader that binary breakup drives any initial mosaic toward an irregular primitive mosaic with cuboid averages (*SI Appendix*, section 1)—emphasizing the strength of the Platonic attractor.

Geometry of Natural 3D Fragments. Based on the pattern generator (Fig. 5), we expect that natural 3D fragments should have cuboid properties on average, $[\bar{f}, \bar{v}] = [6, 8]$. To test this, we collected 556 particles from the foot of a weathering dolomite rock outcrop (Fig. 6) and measured their values of f and v, plus mass and additional shape descriptors (*Materials and Methods* and *SI Appendix*, section 5) (54). We found striking agreement: The measured averages $[\bar{f}, \bar{v}] = [6.63, 8.93]$ were within 12% of the theoretical prediction, and distributions for f and v were centered around the theoretical values. Moreover, odd values for v were much less frequent than even values, illustrating that natural fragments are well approximated by simple polyhedra (Fig. 6). We regard these results as direct confirmation of the hypothesis, while also recognizing significant variability in the natural data.

To better understand the full distributions of fragment shapes, we used geometric simulations of regular and irregular primitive mosaics. The *cut model* simulated regular primitive mosaics as primary fracture patterns by intersecting an initial cube with global planes (Fig. 6), while the *break model* simulated irregular primitive mosaics resulting from secondary fragmentation processes. We fit both of these models to the shape descriptor data using three parameters: one for the cutoff in the mass distribution and two accounting for uncertainty in experimental protocols (*Materials and Methods* and *SI Appendix*, section 5). The best-fit model, which corresponds to a moderately irregular primitive mosaic, produced topological shape distributions that are very close to those of natural fragments (mean values $[\bar{f}, \bar{v}] = [6.58, 8.74]$). We also analyzed a much larger, previously collected dataset (3,728 particles) containing a diversity of materials and formative conditions (19). Although values for v and f were not reported, measured values for classical shape descriptors (19, 21) could be used to fit to the cut and break models (*SI Appendix*, section 5). We found very good agreement ($R^2 > 0.95$), providing further evidence that natural 3D fragments are predominantly formed by binary breakup (*SI Appendix*, Fig. S12). Finally, we used the cut model to demonstrate how 3D primitive fracture mosaics converge asymptotically toward the Platonic attractor as more fragments are produced (Fig. 6).

Discussion and Implications

The application and extension of the theory of convex mosaics provides a lens to organize all fracture mosaics—and the fragments they produce—into a geometric global chart. There are attractors in this global chart, arising from the mechanics of fragmentation. The Platonic attractor prevails in nature because

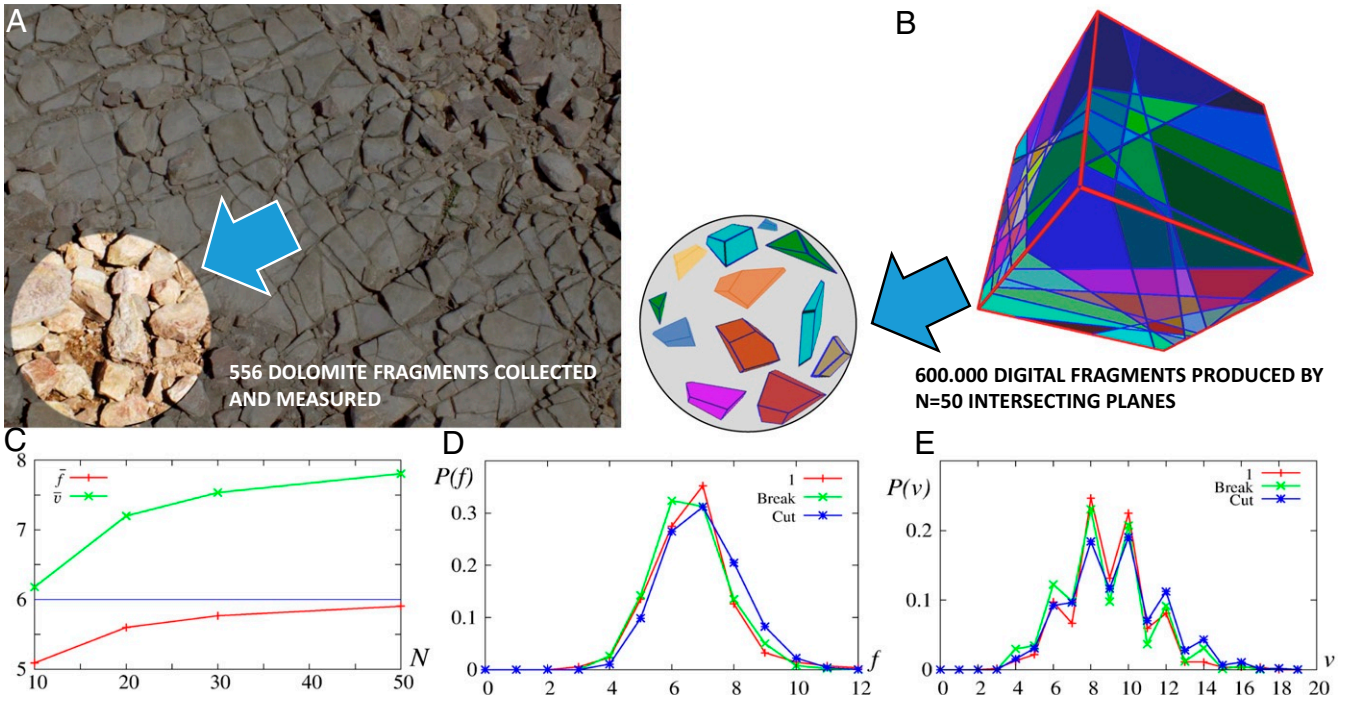

Fig. 6. Natural rock fragments and geometric modeling. (*A*) Dolomite rock outcrop at Hármashatárhegy, Hungary, from which we sampled and measured natural fragments accumulating at its base, highlighted in *Inset*. (*B*) The cut model shown with $N = 50$ intersecting planes and examples of digital fragments (*Inset*) drawn from the 600,000 fragments produced. (*C*) Evolution of the face and vertex number averages $\bar{f}$ and $\bar{v}$, showing convergence toward the cuboid values of eight and six, respectively, with increasing N. (*D* and *E*) Probability distributions of f and v, respectively, for natural dolomite fragments and fits of the cut and break models (for details on the latter, see main text).

binary breakup is the most generic fragmentation mechanism, producing averages corresponding to quadrangle cells in 2D and cuboid cells in 3D. Remarkably, a geometric model of random intersecting planes can accurately reproduce the full shape distribution of natural rock fragments. Our findings illustrate the remarkable prescience of Plato's cubic Earth model. One cannot, however, directly "see" Plato's cubes; rather, their shadows are seen in the statistical averages of many fragments. The relative rarity of other mosaic patterns in nature make them exceptions that prove the rule. Voronoi mosaics are a second important attractor in 2D systems such as mud cracks, where hydrostatic tension or healing of fractures forms hexagonal cells. Such conditions are rare in natural 3D systems. Accordingly, columnar mosaics arise only under specific stress fields that are consistent with iconic basalt columns experiencing contraction under directional cooling. The 3D Voronoi mosaics require very special stress conditions, 3D hydrostatic tension, and may describe rare and poorly understood concretions known as septarian nodules.

We have shown that Earth's Tectonic Mosaic has a geometry that is consistent with what is known about fragmentation related to plate tectonics (5) (Fig. 3). This opens the possibility of constraining stress history from observed fracture mosaics. Space missions are accumulating an ever-growing catalog of 2D and 3D fracture mosaics from diverse planetary bodies that challenge understanding (Fig. 1). Geometric analysis of surface mosaics may inform debates on planetary dynamics, such as whether Pluto's polygonal surface (Fig. 1*C*) is a result of brittle fracture or vigorous convection (7). Another potential application is using 2D outcrop exposures to estimate the 3D statistics of joint networks in rock masses, which may enhance prediction of rockfall hazards and fluid flow (55). While the present work focused on the shapes of fragments, the theory of convex mosaics (39) is also capable of predicting particle-size distributions resulting from fragmentation, which may find application in a wide range of geophysical problems.

The life cycle of sedimentary particles is a remarkable expression of geometry in nature. Born by fragmentation (19) as statistical shadows of an invisible cube, and rounded during transport along a universal trajectory (56), pebble shapes appear to evolve toward the likewise invisible gömböc—albeit without reaching that target (57). The mathematical connections among these idealized shapes, and their reflections in the natural world, are both satisfying and mysterious. Further scrutiny of these connections may yet unlock other surprising insights into nature's shapes.

Methods of Mechanical Simulations

Initial samples were randomized cubic assemblies of spheres glued together, with periodic boundary conditions in all directions. The glued contact was realized by a flat, elastic cylinder connecting the two particles, which was subject to deformation from the relative motion of the glued particles. Forces and torques on the particles were calculated based on the deformation of the gluing cylinder. The connecting cylinder broke permanently if the stress acting upon it exceeded the Tresca criterion (53). The stress field was implemented by slowly deforming the underlying space. In order to avoid that there is only one percolating crack, we set a strong viscous friction between the particles and the underlying space. The seeding for the evolving cracks was provided by the randomized initial geometry of the spheres. This acted as a homogeneous drag to the particles, which ensured a homogeneous stress field in the system.

For any given shear rate, the fragment size is controlled by the particle space viscosity and the Tresca criterion limit. We set values that produced reasonable-sized fragments relative to our computational domain, allowing us to characterize the mosaics. Another advantage of the periodic system was that we could avoid any wall effect that would distort the stress field. We note here that it is possible to slowly add a shear component to the isotropic tensile shear test and obtain a structure which has average values of $\bar{n}$ and $\bar{v}$ that are between the primitive mosaics and the Voronoi case. Details of mechanical simulations are discussed in *SI Appendix*, section 4.

Materials and Methods

Methods for Fitting Geometric Model Results to Field Data. In the simulation, we first computed a regular primitive mosaic by dissecting the unit cube with 50 randomly chosen planes, resulting in 6×10^5 fragments. We refer to this simulation as the *cut model*. Subsequently, we further evolved the mosaic by breaking individual fragments. We implemented a standard model of binary breakup (14, 19) to evolve the cube by secondary fragmentation: At each step of the sequence, fragments either break with a probability p_b into two pieces or keep their current size until the end of the process with a probability $1 - p_b$. The cutting plane was placed in a stochastic manner by taking into account that it is easier to break a fragment in the middle perpendicular to its largest linear extent. Inspired by similar computational models (19), we used p_b dependent on axis ratios (*SI Appendix*, section 5). This computation, which we call the *break model*, provides an approximation to an irregular primitive mosaic; this secondary fragmentation process influenced the nodal degree $\bar{n}$, but not $[\bar{v}, \bar{f}]$.

In order to compare numerical results with the experimental data obtained by manual measurements, we have to take into account several sampling biases. First, there is always a lower cutoff in size for the experimental samples. We implemented this in simulations by selecting only fragments with $m > m_0$, m_0 being the cutoff threshold. Second, there is experimental uncertainty when determining shape descriptors—especially marginally stable or unstable equilibria for the larger dataset (*SI Appendix*, section 5). We implemented this in the computations by letting the location of the center of mass be a random variable with variation σ_0 chosen to be small with respect to the smallest diameter of the fragment. We kept only those equilibria which were found in 95% of the cases. Third, there is experimental uncertainty in finding very small faces. We implemented this into the computations by assuming that faces smaller than A_0P will not be found by experimenters, where P denotes the smallest projected area of the fragment. Using the above three parameters, we fitted the seven computational histograms to the seven experimental ones by minimizing the largest deviation, and we achieved matches with $R^2_{\max} \geq 0.95$ from all histograms (see *SI Appendix*, section 5 for details). Results for the small dataset are shown in Fig. 6.

Data Availability. Shape and mass data for all measured 3D rock fragments, including both the small and large experimental datasets, are freely available at https://osf.io/h2ezc/. All code for the geometric simulations—i.e., the cut and break models—is free to download from https://github.com/torokj/Geometric_fragmentation.

ACKNOWLEDGMENTS. We thank Zsolt Lángi for mathematical comments; Krisztián Halmos for invaluable help with field data measurements; Andrew Gunn for careful review of the figures; and David J. Furbish and Mikael Attal, whose comments helped to improve the manuscript substantially. This research was supported by Hungarian National Research, Development, and Innovation Office Grants K134199 (to G.D.), K116036 (to J.T.), and K119967 (to F.K.); Hungarian National Research, Development, and Innovation Office TKP2020 IE Grant BME Water Sciences & Disaster Prevention (to G.D. and J.T.); US Army Research Office Contract W911NF-20-1-0113 (to D.J.J.); and US NSF National Robotics Initiative INT Award 1734355 (to D.J.J.).

1. D. L. Turcotte, *Fractals and Chaos in Geology and Geophysics* (Cambridge University Press, Cambridge, UK, 1997).
2. H. Kawamura, T. Hatano, N. Kato, S. Biswas, B. K. Chakrabarti, Statistical physics of fracture, friction, and earthquakes. *Rev. Mod. Phys.* **84**, 839–884 (2012).
3. P. M. Adler, J. F. Thovert, *Fractures and Fracture Networks* (Springer, Dordrecht, Netherlands, 1999).
4. C. L. Prasher, *Crushing and Grinding Process Handbook* (John Wiley & Sons, New York, NY, 1987).
5. C. Mallard, N. Coltice, M. Seton, R. D. Müller, P. J. Tackley, Subduction controls the distribution and fragmentation of Earth's tectonic plates. *Nature* **535**, 140–143 (2016).
6. A. S. McEwen, Tidal reorientation and the fracturing of Jupiter's moon Europa. *Nature* **321**, 49–51 (1986).

7. A. Trowbridge, H. Melosh, J. Steckloff, A. Freed, Vigorous convection as the explanation for Pluto's polygonal terrain. *Nature* **534**, 79–81 (2016).
8. J. N. Cuzzi *et al.*, An evolving view of Saturn's dynamic rings. *Science* **327**, 1470–1475 (2010).
9. L. Brooker *et al.*, Clastic polygonal networks around Lyot Crater, Mars: Possible formation mechanisms from morphometric analysis. *Icarus* **302**, 386–406 (2018).
10. N. Brilliantov *et al.*, Size distribution of particles in Saturn's rings from aggregation and fragmentation. *Proc. Natl. Acad. Sci. U.S.A.* **112**, 9536–9541 (2015).
11. G. Domokos, Z. Lángi, Plato's error and a mean field formula for convex mosaics. *Axiomathes*, https://doi.org/10.1007/s10516-019-09455-w (2019).
12. Plato, *Timaeus.* Translated by B. Jowett (Aeterna Press, London, UK, 2015).
13. B. Grünbaum, Uniform tilings of 3-space. *Geombinatorics* **4**, 49–56 (1994).
14. T. Ishii, M. Matsushita, Fragmentation of long thin glass rods. *J. Phys. Soc. Jpn.* **61**, 3474–3477 (1992).
15. L. Oddershede, P. Dimon, J. Bohr, Self-organized criticality in fragmenting. *Phys. Rev. Lett.* **71**, 3107–3110 (1993).
16. F. K. Wittel, F. Kun, H. J. Herrmann, B. H. Kröplin, Fragmentation of shells. *Phys. Rev. Lett.* **93**, 035504 (2004).
17. G. Timár, J. Blömer, F. Kun, H. J. Herrmann, New universality class for the fragmentation of plastic materials. *Phys. Rev. Lett.* **104**, 095502 (2010).
18. F. Kun, F. K. Wittel, H. J. Herrmann, B. H. Kröplin, K. J. Maloy, Scaling behaviour of fragment shapes. *Phys. Rev. Lett.* **96**, 025504 (2006).
19. G. Domokos, F. Kun, A. A. Sipos, T. Szabó, Universality of fragment shapes. *Sci. Rep.* **5**, 9147 (2015).
20. G. Ma, W. Zhou, Y. Zhang, Q. Wang, X. Chang, Fractal behavior and shape characteristics of fragments produced by the impact of quasi-brittle spheres. *Powder Technol.* **325**, 498–509 (2018).
21. T. Szabó, G. Domokos, J. P. Grotzinger, D. J. Jerolmack, Reconstructing the transport history of pebbles on Mars. *Nat. Commun.* **6**, 8366 (2015).
22. S. Steacy, C. Sammis, An automaton for fractal patterns of fragmentation. *Nature* **353**, 250–252 (1991).
23. J. A. Astrom, F. Ouchterlony, R. P. Linna, J. Timonen, Universal dynamic fragmentation in d dimensions. *Phys. Rev. Lett.* **92**, 245506 (2004).
24. W. Dershowitz, H. Einstein, Characterizing rock joint geometry with joint system models. *Rock Mech. Rock Eng.* **21**, 21–51 (1988).
25. L. Goehring, Evolving fracture patterns: Columnar joints, mud cracks and polygonal terrain. *Phil. Trans. Math. Phys. Eng. Sci.* **371**, 20120353 (2013).
26. X. Ma, J. Lowensohn, J. C. Burton, Universal scaling of polygonal desiccation crack patterns. *Phys. Rev.* **99**, 012802 (2019).
27. L. Goehring, A. Nakahara, T. Dutta, S. Kitsunezaki, S. Tarafdar, *Desiccation Cracks and Their Patterns: Formation and Modelling in Science and Nature* (John Wiley & Sons, New York, NY, 2015).
28. L. Goehring, R. Conroy, A. Akhter, W. J. Clegg, A. F. Routh, Evolution of mud-crack patterns during repeated drying cycles. *Soft Matter* **6**, 3562–3567 (2010).
29. A. Aydin, J. M. Degraff, Evolution of polygonal fracture patterns in lava flows. *Science* **239**, 471–476 (1988).
30. E. A. Jagla, A. G. Rojo, Sequential fragmentation: The origin of columnar quasihexagonal patterns. *Phys. Rev. E* **65**, 026203 (2002).
31. M. Hofmann, R. Anderssohn, H. A. Bahr, H. J. Weiß, J. Nellesen, Why hexagonal basalt columns? *Phys. Rev. Lett.* **115**, 154301 (2015).
32. H. J. Cho, N. B. Lu, M. P. Howard, R. A. Adams, S. S. Datta, Crack formation and self-closing in shrinkable, granular packings. *Soft Matter* **15**, 4689–4702 (2019).
33. J. S. Clair *et al.*, Geophysical imaging reveals topographic stress control of bedrock weathering. *Science* **350**, 534–538 (2015).
34. A. Voigtländer, M. Krautblatter, Breaking rocks made easy. blending stress control concepts to advance geomorphology. *Earth Surf. Process. Landforms* **44**, 381–388 (2019).
35. P. Molnar, R. S. Anderson, S. P. Anderson, Tectonics, fracturing of rock, and erosion. *J. Geophys. Res.: Earth Surface* **112**, F03014 (2007).
36. R. A. DiBiase, M. W. Rossi, A. B. Neely, Fracture density and grain size controls on the relief structure of bedrock landscapes. *Geology* **46**, 399–402 (2018).
37. L. S. Sklar *et al.*, The problem of predicting the size distribution of sediment supplied by hillslopes to rivers. *Geomorphology* **277**, 31–49 (2017).
38. D. Bahat, A. Rabinovitch, V. Frid, *Tensile Fracturing in Rocks* (Springer-Verlag, Berlin, Germany, 2005).
39. R. Schneider, W. Weil, *Stochastic and Integral Geometry* (Springer Science & Business Media, New York, NY, 2008).
40. K Mills, *Fractography* (ASM Handbook, ASM International, Cleveland, OH, 1991), vol. 12.
41. D. Bahat, V. Rabinovitch, A. Frid, *Tensile Fracturing in Rocks* (Springer, Berlin, Germany, 2005).
42. G. Domokos, Z. Lángi, On some average properties of convex mosaics. *Exp. Math.*, 10.1080/10586458.2019.1691090 (2019).
43. S. Bohn, L. Pauchard, Y. Couder, Hierarchical crack pattern as formed by successive domain divisions. *Phys. Rev. E.* **71**, 046214 (2005).
44. D. L. Anderson, How many plates?*Geology* **30**, 411–414 (2002).
45. P. Bird, An updated digital model of plate boundaries. *Geochem., Geophys., Geosyst.* **4**, 1027 (2003).
46. G. Hernández, H. J. Herrmann, Discrete models for two- and three-dimensional fragmentation. *Physica A* **215**, 420–430 (1995).
47. P. Kekalainen, J. A. Aström, J. Timonen, Solution for the fragment-size distribution in a crack-branching model of fragmentation. *Phys. Rev. E* **76**, 026112 (2007).
48. A. Lamur *et al.*, Disclosing the temperature of columnar jointing in lavas. *Nat. Commun.* **9**, 1432 (2018).
49. JR Boles, C. A. Landis, P. Dale, The Moeraki Boulders; anatomy of some septarian concretions. *J. Sediment. Res.* **55**, 398–406 (1985).
50. T. Astin, Septarian crack formation in carbonate concretions from shales and mudstones. *Clay Miner.* **21**, 617–631 (1986).
51. D. Flinn, On folding during three dimensional progressive deformation. *Quart. Journ. Geol. Soc. London* **118**, 385–428 (1962).
52. S. Plimpton, Fast parallel algorithms for short-range molecular dynamics. *J. Comput. Phys.* **117**, 1–19 (1995).
53. L. Brendel, J. Török, R. Kirsch, U. Bröckel, A contact model for the yielding of caked granular materials. *Granul. Matter* **13**, 777–786 (2011).
54. J. Török, G. Domokos, Geometric descriptors of fragments. Open Science Framework. https://osf.io/h2ezc/. Deposited 2 April 2020.
55. National Research Council, *Rock Fractures and Fluid Flow: Contemporary Understanding and Applications* (National Academies Press, Washington, DC, 1996).
56. T. Novák-Szabó *et al.*, Universal characteristics of particle shape evolution by bed-load chipping. *Sci. Adv.* **4**, eaao4946 (2018).
57. G. Domokos, Natural numbers, natural shapes. *Axiomathes*, 10.1007/s10516-018-9411-5 (2018).
58. J. Corominas, O. Mavrouli, R. Ruiz-Carulla, "Rockfall occurrence and fragmentation" in *Advancing Culture of Living with Landslides*, K. Sassa, M. Mikoš, Y. Yin, Eds. (Springer International Publishing, Cham, Switzerland, 2017), pp. 75–97.